One-dimensional Bose gas on an atom chip

van Amerongen, A.H.

5 Focusing phase-fluctuating condensates

5.1 Introduction

The term 'atom optics' stems from the possibility to translate techniques and theory from optics to the field of atomic physics. Work with atomic and molecular beams dates back to the first half of the twentieth century [132]. Paul and Friedburg [133, 134] first implemented optical imaging with neutral atoms in 1950. Early examples of the exchange of roles of light and matter are the idea by Balykin and Letokhov to focus an atomic beam using an optical potential [135] and their experimental demonstration of the reflection of atoms on an evanescent light wave mirror [136]. Such a light mirror was later used in Amsterdam with the aim of creating a BEC with all optical means [137, 138]. With the achievement of BECs as a source of coherent atomic waves, the step to the experimental demonstration of an atom laser was small [139–142]. Immanuel Bloch and coworkers demonstrated a variety of atom-optical manipulations: reflection, focusing, and the storage of an atom laser beam in a resonator [143]. In the last decade, the group of Alain Aspect made detailed progress in the study of atom lasers [144–148]. A theoretical treatment of the propagation of atom-laser beams was given by Bordé [149, 150]. Coherent atomic waves are a promising tool, analogous to lasers, but with the possibility of a much smaller wavelength and therefore higher spatial resolution. A further application is the use of atomic waves in a Sagnac interferometer that can lead to huge sensitivity improvements over ring laser gyroscopes. The Sagnac phase shift of a particle traversing an interferometer is proportional to the mass energy of the interfering particle, this is 10^{10} times larger for an atom than for a photon [151]. Dave Pritchard and his group performed pioneering experiments using an atomic beam for interferometry [152] in the early 1990s.

Another optical technique applied to atoms was demonstrated in Amsterdam, where a non-equilibrium BEC was focused in free flight [127]. We have extended this atom-focusing technique, also building on the work in Ref. [153], to equilibrium clouds, that are in the cross-over from the three-dimensional to the one-dimensional regime. We have used the technique to study the axial momentum distribution of these gases. In this chapter we present data showing the focusing of clouds in the quasi-condensate regime. We are able to extract the temperature from the focal width of quasi-condensates. In this way we have implemented a novel tool

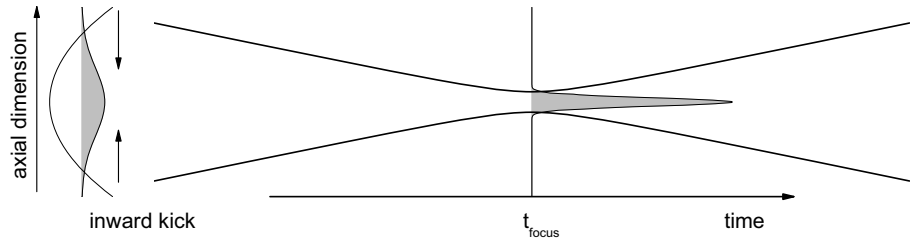

Figure 5.1: Principle of focusing an atomic cloud. We apply a short, strong axial harmonic potential yielding a kick to the atoms proportional to their distance from the trap center, followed by free propagation. As a result the atoms come to a focus, at which time (t_{focus}) the axial density distribution reflects the axial momentum distribution before focusing.

for cold atom thermometry. We derive the relation between the focal width and the temperature by explicitly exploiting the wave nature of atoms: An elongated (quasi-)condensate as it propagates freely after its release from the trap is described as a macroscopic wavefunction. It obeys the Schrödinger equation that has the same form as the paraxial wave equation for light.

We have also obtained focusing results for cold clouds in a regime where atomic interactions and non-zero temperature lead to reduced coherence, and a quasi-condensate description is not always applicable. Those results are described in Ch. 6.

The concept of focusing an elongated cloud is as follows: We apply a short, strong axial harmonic potential yielding a kick to the atoms proportional to their distance from the trap center (analogous to the action of a lens in optics), followed by free propagation. As a result the atoms come to a focus, at which time (t_{focus}) the axial density distribution reflects the axial momentum distribution before focusing. The focusing concept is illustrated in Fig. 5.1. Since the focusing brings all atoms together axially, the signal level is high, even for a single realization. As we will show, averaging over a few shots is sufficient to obtain high signal-to-noise ratio.

The outline of this chapter is as follows. We start in Sec. 5.2 by giving a brief summary of concepts known from optics like the ABCD matrix, the Huygens-Fresnel integral and gaussian beam propagation. We proceed in Sec. 5.3 by exploiting the equivalence of the paraxial wave equation and the Schrödinger equation in 1D to outline the theory for matter wave propagation through linear ABCD systems. We extend the existing work on nonideal light beams [154, 155] and matter wave propagation [146, 148–150] by making a connection between the quality factor M^2 of a nonideal atomic beam and the temperature of a quasi-condensate. This treatment enables us to derive the relation between the focal width of quasi-condensates and the temperature, given in Sec. 5.4. In Sec. 5.5 we summarize the behavior of a weakly interacting quasi-condensate in a time-dependent trap with scaling equations [156–158]. The experimental methods and results of the novel quasi-condensate thermometry method are presented in Sec. 5.6. In Sec. 5.7 we discuss the experimental limits of the presented method. We conclude this chapter and give an outlook in Sec. 5.8.

5.2 Gaussian and nonideal optical beams and ABCD matrices

As an introduction to *atom optics* some basics of gaussian beam optics and ABCD matrices are briefly summarized following Ref. [124]. Additionally, we discuss the treatment of nonideal light beams, using the quality factor M^2 that was developed by Siegman [159] and Bélanger [160] in the early 1990s.

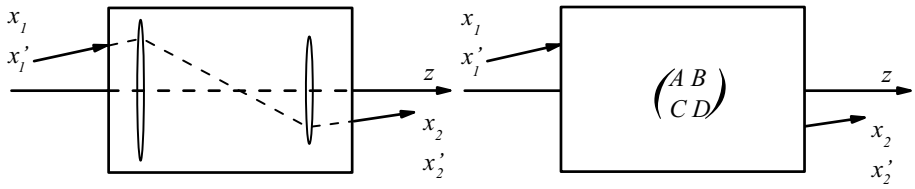

Figure 5.2: Overall ABCD matrix for the propagation of an optical ray through a cascade of optical elements.

In textbook optics [161, 162] an ABCD matrix describes the transformation of the vector of position x and slope x' of a light ray as it propagates from a plane z_1 to a plane z_2 through a cascade of optical elements as is shown in Fig. 5.2. In matrix form

$$\begin{pmatrix} x_2 \\ x_2' \end{pmatrix} = \begin{pmatrix} A & B \\ C & D \end{pmatrix} \begin{pmatrix} x_1 \\ x_1' \end{pmatrix}. \tag{5.1}$$

The ABCD matrix has unit determinant

$$AD - BC = 1. \tag{5.2}$$

For a complete system, with many elements, the overall ABCD ray matrix is simply computed by multiplication of matrices of the individual optical elements and regions of free space that a light ray passes.

5.2.1 Paraxial wave equation and Huygens-Fresnel integral

We consider a monochromatic light wave that propagates mainly along the optical axis and has a slowly varying envelope. We write the general complex wave like

$$\tilde{E}(x, y, z) \equiv \tilde{u}(x, y, z)e^{ikz}, \tag{5.3}$$

where $k = 2\pi/\lambda$ is the wavevector of the light.[1] The propagation of this beam is governed by the electromagnetic wave equation that follows from Maxwell's equations and the appropriate boundary conditions. In the wave equation the second partial derivative in z may be dropped if

$$\left|\frac{\partial^2 \tilde{u}}{\partial z^2}\right| \ll \min\left\{\left|2k\frac{\partial \tilde{u}}{\partial z}\right|, \left|\frac{\partial^2 \tilde{u}}{\partial x^2}\right|, \left|\frac{\partial^2 \tilde{u}}{\partial y^2}\right|\right\}. \tag{5.4}$$

[1] We use the imaginary number i instead of $-j$ used by Siegman.

The propagation of $\tilde{u}(x, y, z)$ in free space can then be described with the *paraxial wave equation* in the form

$$\left[\nabla_{\mathbf{r}}^2 + 2ik\frac{\partial}{\partial z}\right]\tilde{u}(\mathbf{r}, z) = 0, \tag{5.5}$$

where $\mathbf{r} \equiv (x, y)$ are the transverse coordinates and $\nabla_{\mathbf{r}}$ is the laplacian operator working on these transverse directions. The paraxial wave approximation is valid if the inequality (5.4) is satisfied. This is typically applicable for waves that propagate at an angle of less than 30° with the optical axis [124].

The propagation of paraxial beams can be calculated alternatively using Huygens' integral. A wave (writing only one transverse dimension for brevity) $\tilde{u}(x)$ is transported from the plane z_1 to the plane z_2 by

$$\tilde{u}(x_2) = \int_{-\infty}^{\infty} \mathcal{K}(x_2, x_1)\tilde{u}(x_1)dx_1, \tag{5.6}$$

where $\mathcal{K}(x_2, x_1)$ is the Huygens kernel. If the criterium (5.4) is met, it can be written in the Fresnel approximation

$$\mathcal{K}(x_2, x_1) = \frac{1}{\sqrt{2i\pi B}} \exp\left[\frac{i}{2B}(Ax_1^2 - 2x_2x_1 + Dx_2^2)\right], \tag{5.7}$$

where, for a given optical system A, B and D are the same constants that appear in the ABCD matrix of that system derived using geometric optics, Eq. (5.1) and Eq. (5.2). By inserting Eq. (5.7) in Eq. (5.6) we get the Huygens-Fresnel integral

$$\tilde{u}(x_2) = \int_{-\infty}^{\infty} \frac{1}{\sqrt{2i\pi B}} \exp\left[\frac{i}{2B}(Ax_1^2 - 2x_2x_1 + Dx_2^2)\right]\tilde{u}(x_1)dx_1. \tag{5.8}$$

A set of solutions to both the paraxial wave equation and the Huygens-Fresnel integral is formed by the gaussian beams of the form

$$\tilde{u}(x, z) = \tilde{q}\exp\left[ik\frac{x^2}{2R(z)} - \frac{x^2}{w^2(z)}\right], \tag{5.9}$$

we have used the complex radius of curvature, defined as

$$\frac{1}{\tilde{q}} \equiv \frac{1}{R(z)} + i\frac{\lambda}{\pi w^2(z)}, \tag{5.10}$$

where $R(z)$ is the radius of curvature and $w(z)$ is the $1/e^2$ intensity half width. The variation of the complex radius of curvature along z is

$$\tilde{q}(z) = \tilde{q}_0 + z - z_0, \tag{5.11}$$

with the complex source point $\tilde{q}_0 = \tilde{q}(z_0)$. This leads to

$$w^2(z) = w_0^2\left[1 + \frac{(z - z_0)^2}{z_R^2}\right], \tag{5.12}$$

with w_0 the minimum transverse size, and

$$R(z) = z + \frac{z_R^2}{z}. \tag{5.13}$$

Where the Rayleigh range

$$z_R \equiv \frac{\pi w_0^2}{\lambda}, \tag{5.14}$$

is the distance the beam travels from the waist w_0 until the diameter increases by a factor $\sqrt{2}$. It is shown for example in [124] using the Huygens-Fresnel integral [Eq. (5.8)] that for a general system characterized by an ABCD matrix the complex beam parameter $\tilde{q}$ transforms according to the relation

$$\tilde{q}_2 = \frac{A\tilde{q}_1 + B}{C\tilde{q}_1 + D}. \tag{5.15}$$

Thus a gaussian beam can be propagated through cascaded optical elements using the cascaded ABCD matrix for those elements.

5.2.2 Nonideal beam

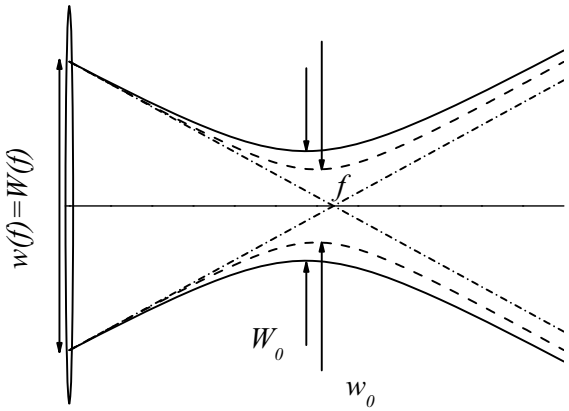

Figure 5.3: Focusing of a Gaussian light beam (dashed line) and a nonideal light beam (solid line) with the same size at the lens position but $M^2 = 1.5$; the dash dotted line intersects the axis at the geometrical focus f of the lens.

To treat monochromatic beams in the paraxial approximation that are *not* diffraction limited and have ripples in phase and amplitude at any transverse plane, Siegman [159] and Bélanger [160] have introduced a treatment analogous to that for gaussian beams. Consider a beam size $W(z)^2 \equiv [2\Delta x(z)]^2$, where Δx^2 is the second-order moment [Eq. (5.30)] of the transverse intensity profile of the general beam. The complex radius of curvature can be generalized for arbitrary beams [159]

$$\frac{1}{Q} = \frac{1}{R} + i\frac{\lambda M^2}{\pi W^2}, \tag{5.16}$$

where R approximates the mean radius of curvature and M^2 is the so-called beam quality factor that is an invariant coefficient of the beam. Just like for gaussian beams, it follows from the Huygens-Fresnel integral [Eq. (5.8)] that the generalized radius of curvature for an arbitrary beam obeys the relation [160]

$$Q_2 = \frac{AQ_1 + B}{CQ_1 + D}. \tag{5.17}$$

This formalism now allows the propagation of arbitrary paraxial beams through ABCD systems. As a simple example we write the propagation rule for the beam size of an arbitrary beam as it propagates through free space starting from its waist at z_0 where the beam attains its minimum size W_0

$$W^2(z) = W_0^2 \left[1 + M^4 \left(\frac{\lambda}{\pi W_0^2} \right)^2 (z - z_0)^2 \right]. \tag{5.18}$$

A comparison of an ideal gaussian beam and a distorted beam with $M^2 = 1.5$ is plotted in Fig. 5.3.

5.3 Atom optics and ABCD matrices

In this section the step from *light optics* to *atom optics* is made. In Sec. 5.3.1 the equivalence of the paraxial wave equation and Schrödinger's equation for matter waves is discussed. Further, via the Huygens-Fresnel integral applied to matter waves we arrive in Sec. 5.3.2 at a formulation of the ABCD matrices for atoms. In Sec. 5.3.3 we relate the temperature of a non-interacting gas to its focal width.

5.3.1 Schrödinger equation and Wigner function

The application of techniques from optics to matter waves can be established by exploiting the analogy between the paraxial wave equation for light Eq. (5.5) and the Schrödinger equation for matter waves:

$$\left[\frac{\hbar^2}{2m} \nabla_x^2 + i\hbar \frac{\partial}{\partial t} + V_{\text{ext}}(x) \right] \psi(x,t) = 0. \tag{5.19}$$

As in Sec. 5.2 we restrict ourselves here to one single transverse dimension. Note that the Schrödinger equation Eq. (5.19) is equivalent to the paraxial wave equation [Eq. (5.5)] with the correspondences [149]:

$$t \longleftrightarrow z, \quad \frac{m}{\hbar} \longleftrightarrow k, \quad V_{\text{ext}} \longleftrightarrow 0, \quad \psi \longleftrightarrow \tilde{u}. \tag{5.20}$$

In the Schrödinger equation the wavefunction $\Psi(x,t)$ propagates in time equivalently to the wavefront $\tilde{u}(x,z)$ along the axis z. Additionally, for a wave propagating in a medium with refractive index $n(x) = n_0 - n_2 x^2/2$, as in a "duct" (see [124] p. 652 and

the Errata) the correspondence for a harmonic oscillator potential $V_{\text{ext}} = m\omega^2 x^2/2$ is

$$\omega^2 \longleftrightarrow \frac{n_2}{n_0}. \tag{5.21}$$

Because of this equivalence, the ABCD matrix formalism and the Huygens-Fresnel integral can also be applied to the wavefunction Ψ to calculate its propagation through a cascade of harmonic potentials and sections of free space.

Let us look at a matter wave $\Psi(x,t)$ obeying Eq. (5.19) with, in general, a distorted density and phase distribution. The distribution in momentum[2] space $\bar{\Psi}(k)$ can be found by taking the Fourier transform of $\Psi(x)$, defined as

$$\bar{\Psi}(k) = \frac{1}{\sqrt{2\pi}} \int_{-\infty}^{\infty} \Psi(x) e^{-ikx} dx. \tag{5.22}$$

Before continuing with the ABCD formalism for matter waves, it is useful to briefly digress and introduce the Wigner distribution function (WDF). The Wigner distribution function $W(x,k)$ characterizes the state of a quantum system in phase space [154, 163–165]

$$W(x,k,t) \equiv \frac{1}{2\pi} \int_{-\infty}^{\infty} \Psi(x + x'/2, t) \Psi^*(x - x'/2, t) e^{-ikx'} dx', \tag{5.23}$$

were * denotes the complex conjugate. The projections of the WDF have a physical meaning. The density distribution is

$$\int_{-\infty}^{\infty} W(x,k,t) dk = |\Psi(x,t)|^2, \tag{5.24}$$

and the momentum distribution is

$$\int_{-\infty}^{\infty} W(x,k,t) dx = |\bar{\Psi}(k,t)|^2. \tag{5.25}$$

The integral over the whole Wigner chart yields the total probability, equal to 1 for a normalized wavefunction

$$\int_{-\infty}^{\infty} \int_{-\infty}^{\infty} W(x,k,t) dx dk = 1. \tag{5.26}$$

Unless stated otherwise we will indeed take W (and Ψ) to be normalized in this way.

The Huygens-Fresnel integral [Eq. (5.8)] acts on the Wigner distribution function as a coordinate transformation. Specifically, let two functions $f(x)$ and $g(x)$ be related by the Huygens-Fresnel integral. Then the Wigner functions of $f(x)$ and $g(x)$ are related by [155]

$$W_g(x_2, k_2) = W_f(x_1, k_1), \tag{5.27}$$

[2]For notational convenience we actually use the wavevector k instead of the momentum $p = \hbar k$. Note for instance that the phase space area $\Delta x \Delta k$ is dimensionless.

where the coordinate transformation can be written in the ABCD form

$$\begin{pmatrix} x_2 \\ k_2 \end{pmatrix} = \begin{pmatrix} A & B \\ C & D \end{pmatrix} \begin{pmatrix} x_1 \\ k_1 \end{pmatrix}. \tag{5.28}$$

In this way we can conveniently express the transformation of a matter wave in phase space when it traverses a system of cascaded potentials represented by the total ABCD matrix.

5.3.2 ABCD matrices for matter waves

The aim of this section is to find the propagation of the second-order moments of a wavepacket through an ABCD system that represents our atom focusing experiment. Part of this section follows the work by Bastiaans [155].

Wigner chart

We start by drawing the simple Wigner chart for a one-dimensional, minimum-uncertainty ("Heisenberg-limited"), atomic wavepacket (with the same mathematical form as an ideal gaussian beam). The wavefunction is

$$\Psi_H(x) = \left(\frac{1}{2\pi\Delta x^2}\right)^{1/4} e^{-x^2/(2\Delta x)^2}. \tag{5.29}$$

The density distribution is symmetric around $x = 0$ (and $k = 0$). In the case $\langle x\rangle = \langle k\rangle = 0$, the second-order moments of the density distribution $\Delta x^2(t)$ and the momentum distribution $\Delta k^2(t)$ are defined as

$$\Delta x^2(t) = \int_{-\infty}^{\infty} x^2 |\Psi(x,t)|^2 dx, \tag{5.30}$$

$$\Delta k^2(t) = \int_{-\infty}^{\infty} k^2 |\bar{\Psi}(k,t)|^2 dk. \tag{5.31}$$

For $\Psi_H(x)$ [Eq. (5.29)] the product $\Delta x\Delta k = 1/2$, indeed the wavepacket is Heisenberg limited. Using this relation and Eq. (5.23) we arrive at the Wigner distribution function of the minimum-uncertainty wavepacket

$$W_H(x,k) = \frac{1}{\pi} e^{-\frac{k^2}{2\Delta k^2} - \frac{x^2}{2\Delta x^2}}. \tag{5.32}$$

A graphical representation of $W_H(x,k)$ is shown in Fig. 5.4.

propagation of second-order moments

In addition to the second-order moments of position and momentum [Eq. (5.30)] it is useful to define a 'mixed moment' Δ_{xk} employing the WDF

$$\Delta_{xk}(t) = \Delta_{kx}(t) = \int_{-\infty}^{\infty}\int_{-\infty}^{\infty} xkW(x,k,t)dxdk, \tag{5.33}$$

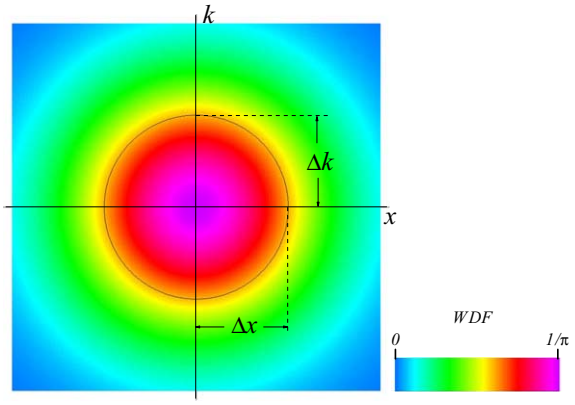

Figure 5.4: The Wigner distribution function (WDF) characterizes the state of a quantum system in phase space. Shown here is the Wigner distribution function of a minimum uncertainty wavepacket.

The propagation of the second-order moments Δx^2, Δk^2, Δ_{xk} and Δ_{kx} of a wavepacket that propagates through an ABCD system, between times t_1 and t_2, is also conveniently written in matrix form [155]

$$\begin{pmatrix} \Delta x^2(t_2) & \Delta_{kx}(t_2) \\ \Delta_{xk}(t_2) & \Delta k^2(t_2) \end{pmatrix} = \begin{pmatrix} A & B \\ C & D \end{pmatrix} \begin{pmatrix} \Delta x^2(t_1) & \Delta_{kx}(t_1) \\ \Delta_{xk}(t_1) & \Delta k^2(t_1) \end{pmatrix} \begin{pmatrix} A & B \\ C & D \end{pmatrix}^T. \quad (5.34)$$

The ABCD matrices have unit determinant, therefore Eq. (5.34) shows that the determinant of the matrix of moments at t_2 equals that at t_1: The determinant is an invariant of the propagation in this system

$$\Delta x^2(t)\Delta k^2(t) - \Delta_{xk}(t)\Delta_{kx}(t) \equiv \left(\frac{M^2}{2}\right)^2. \quad (5.35)$$

This determinant defines what was called the M^2 factor for matter waves by Riou and coworkers [146, 148].

As an example, we write down M^2 for a classical ideal gas in a harmonic trap. Such a classical Boltzmann gas assumes a gaussian shape in a harmonic potential. Atoms do not interact and the density distribution can be treated separately for each direction. Consider a gas in thermal equilibrium so that the average position and momentum are not related and $\Delta_{xk} = 0$. In the axial direction the position spread is given by

$$\Delta x_T = \sqrt{\frac{k_B T}{m\omega_\parallel^2}}, \quad (5.36)$$

while the Boltzmann gas has a momentum spread

$$\Delta k_T = \frac{1}{\hbar}\sqrt{m k_B T}. \quad (5.37)$$

Equation (5.35) then yields the quality factor for a trapped Boltzmann gas

$$\frac{M^2}{2} = \frac{k_B T}{\hbar\omega_\parallel}. \tag{5.38}$$

Intuitively, it counts the number of thermally occupied modes of the axial harmonic oscillator potential.

Equation (5.34) describes how the second-order moments of a wavepacket propagate through a general ABCD system. The next step is then to write down the ABCD matrices corresponding to the specific transformations in phase space that we encounter in our focusing experiment. The focusing procedure consists of two stages: In the first stage we pulse on the harmonic potential $V(x) = m\omega^2 x^2/2$. In the second stage the magnetic potential is completely switched off, and the wavepacket propagates freely.

harmonic potential ABCD matrix

Consider a classical particle with position x and velocity $p(t)/m = \hbar k(t)/m$ in the harmonic potential $V(x) = m\omega^2 x^2/2$. The particle motion is described by the equations

$$\begin{aligned} \frac{dx}{dt} &= \frac{\hbar k(t)}{m}, \\ \hbar\frac{dk}{dt} &= m\omega^2 x(t). \end{aligned} \tag{5.39}$$

The general solution for the propagation of the particle from a time t_1 to a later time t_2 is

$$x_2 = x_1 \cos\omega t + \frac{\hbar}{m\omega} k_1 \sin\omega t. \tag{5.40}$$

From Eq. (5.40) and its derivative we can see that the ABCD matrix acting on the pair (x, k) is

$$\begin{pmatrix} x_2 \\ k_2 \end{pmatrix} = \begin{pmatrix} \cos\omega t & \frac{\hbar}{m\omega}\sin\omega t \\ -\frac{m\omega}{\hbar}\sin\omega t & \cos\omega t \end{pmatrix} \begin{pmatrix} x_1 \\ k_1 \end{pmatrix} \equiv \mathbf{M}_{\mathrm{C}} \begin{pmatrix} x_1 \\ k_1 \end{pmatrix}. \tag{5.41}$$

To solve the Schrödinger equation for a quantum mechanical particle in a harmonic oscillator potential, Namias [166] has introduced the so-called fractional order Fourier transform (FrFT).[3] To model our focusing potential we write the fractional Fourier transform for matter waves in the matrix representation. The ABCD matrix corresponding to the standard Fourier transform for matter waves acting on the pair (x, k) is

$$\mathbf{M}_{\mathrm{FT}} = \begin{pmatrix} 0 & \hbar/m\omega \\ -m\omega/\hbar & 0 \end{pmatrix}, \tag{5.42}$$

[3]This mathematical method was applied later on in the field of optics by Mendlovic, Ozaktas and Lohmann [167, 168]. These authors made the connection between the fractional Fourier transform and the propagation of waves in a "duct".

with ω the frequency of the harmonic oscillator. The ABCD matrix of a FrFT can be defined as

$$\mathbf{M}_{\mathrm{FrFT}}^{q} = \mathbf{M}_{\mathrm{FT}}, \tag{5.43}$$

so that if $\mathbf{M}_{\mathrm{FrFT}}$ is applied q times, the full Fourier transform is regained. $\mathbf{M}_{\mathrm{FrFT}}$ can be written in the general form that corresponds exactly to the classical matrix in (5.41)

$$\mathbf{M}_{\mathrm{FrFT}} = \mathbf{M}_{\mathrm{C}}, \tag{5.44}$$

where

$$\omega t = p\frac{\pi}{2} = \frac{\pi}{2q},$$

with p the fractional order of the FrFT. We have the full Fourier transform for $p = 1$. The fractional Fourier transform generates a rotation of the Wigner distribution function over an angle ωt in phase space (x, k) with a scaling factor $\hbar/m\omega$ [as is illustrated in Fig. 5.5(b)]. The value $\omega t = \pi/2$ corresponds to the standard Fourier transform that exactly interchanges the role of position and momentum.

free evolution ABCD matrix

Free temporal evolution of a matter wave simply means $k_2 = k_1$ and $x_2 = x_1 + \hbar k t/m$. In ABCD matrix form we write

$$\mathbf{M}_{\mathrm{free}} = \begin{pmatrix} 1 & \hbar t/m \\ 0 & 1 \end{pmatrix}. \tag{5.45}$$

The above matrix is equivalent to the action of the Fresnel transform on the Wigner function. Using Eq. (5.27) we find that free propagation results in a shearing deformation of the Wigner distribution along the x-direction

$$W(x, k, t) = W(x + \frac{\hbar t}{m}k, k, t), \tag{5.46}$$

as is illustrated in Fig. 5.5(c).

From relation (5.34) and using M^2 [Eq. (5.35)] we get for the propagation of $\Delta x^2(t)$ of a wavepacket

$$\Delta x^2(t_2) = A^2\Delta x^2(t_1) + 2AB\Delta_{xk}(t_1) + B^2\frac{(M^2/2)^2}{\Delta x^2(t_1)}. \tag{5.47}$$

Filling in the elements of $\mathbf{M}_{\mathrm{free}}$ and starting from $t = t_{\mathrm{focus}}$, the time of the narrowest width, where $\Delta_{xk} = 0$ we arrive at the equation that describes the free propagation of a matter wave

$$\Delta x^2(t) = \Delta x_0^2\left[1 + M^4\left(\frac{\hbar}{2m\Delta x_0^2}\right)^2(t - t_{\mathrm{focus}})^2\right], \tag{5.48}$$

where we have written $\Delta x(t_{\mathrm{focus}}) \equiv \Delta x_0$ for brevity. This is equivalent to the relation (5.18) when the correspondence (5.20) is used.

atomic wave focusing ABCD matrix

Finally, by multiplying $\mathbf{M}_{\mathrm{FrFT}}$ and $\mathbf{M}_{\mathrm{Free}}$ we obtain the complete ABCD matrix for the focusing of an atomic wave. We apply the magnetic lens in a pulsed fashion with a pulse time t_{p} followed by a free propagation time $t_{\mathrm{free}} \equiv t - t_{\mathrm{p}}$

$$\mathbf{M} = \begin{pmatrix} \cos\omega t_{\mathrm{p}} - t_{\mathrm{free}}\omega \sin\omega t_{\mathrm{p}} & \frac{\hbar}{m\omega}\sin\omega t_{\mathrm{p}} + \frac{\hbar t_{\mathrm{free}}}{m}\cos\omega t_{\mathrm{p}} \\ -\frac{m\omega}{\hbar}\sin\omega t_{\mathrm{p}} & \cos\omega t_{\mathrm{p}} \end{pmatrix}. \tag{5.49}$$

To find the focus time we require $A = 0$

$$t_{\mathrm{focus}} \;=\; t_{\mathrm{p}} + \frac{\cos\omega t_{\mathrm{p}}}{\omega \sin\omega t_{\mathrm{p}}}. \tag{5.50}$$

The scaling time t_{scale} gives the relation between initial velocity and final position

$$B(t_{\mathrm{focus}}) = \frac{\hbar}{m\omega \sin\omega t_p} = \frac{\hbar}{m} t_{\mathrm{scale}}. \tag{5.51}$$

With the above insights, the procedure can be simply extended to also include ramps in the potential of the form $\omega^2(t) = \omega_0^2 + \alpha t$, as is used in the experiments described in Sec. 5.6. This leads to an ABCD matrix similar to (5.49) that can be obtained by integration of Eq. (5.39).

5.3.3 Temperature of a focused non-interacting gas

In the case of a gas of non-interacting particles we can treat each particle separately. We can subsequently calculate the propagation for an ensemble of non-interacting particles through any ABCD system. Specifically, we calculate the width of a thermal ensemble that is focused using our procedure represented by an ABCD matrix such as (5.49). The width of the focused cloud yields the temperature of a gas.

The propagation of point particles in the classical limit is equivalent to the light-ray limit in optics. The gaussian density distribution of the Boltzmann gas along the trap axis is

$$n_l(x) = n_0 \exp\left[-\beta E(x)\right] = n_0 \exp\left[-\frac{1}{2}\beta m \omega_{\parallel}^2 x^2\right], \tag{5.52}$$

where n_0 is the density in the trap center and $\beta = (k_B T)^{-1}$. Using the temporal scaling of the gaussian cloud we find the evolution of the axial density distribution in time

$$n_l(x,t) = \frac{n_0 \Delta x_T}{\Delta\tilde{x}(t)} \exp\left[-\frac{1}{2}\left(\frac{x}{\Delta\tilde{x}}\right)^2\right], \quad \Delta\tilde{x}(t) = \sqrt{\Delta x_T^2 A^2(t) + \Delta k_T^2 B^2(t)}, \tag{5.53}$$

where we have used the matrix elements $A(t)$ and $B(t)$ and the thermal position and momentum spread Δx_T and Δk_T respectively [Eq. (5.36) and Eq. (5.37)].

For the case of a 3D harmonically trapped ideal Bose gas, at a temperature above

degeneracy, the density distribution is given in a semiclassical approximation by Eq. (2.25). It is useful to introduce the axial and radial harmonic oscillator lengths $l_\parallel = \sqrt{\hbar/m\omega_\parallel}$ and $l_\perp = \sqrt{\hbar/m\omega_\perp}$ respectively. We arrive at the linear density n_l along x by integrating Eq. (2.25) over both radial directions

$$n_l(x) = \frac{l_\perp^4}{\Lambda_T^5} g_{5/2}(ze^{-\beta m\omega_\parallel^2 x^2/2}). \tag{5.54}$$

If the cloud is focused in the axial direction we have access to the density n_p in momentum space [obtained after integration of Eq. (2.26)]

$$n_p(p_\parallel) = \frac{l_\perp^4}{m\omega_\parallel \Lambda_T^5} g_{5/2}(ze^{-\beta p_\parallel^2/2m}). \tag{5.55}$$

This momentum distribution translates into a spatial distribution in the focus as a function of the scaling time [as in Eq. (5.51)]

$$n_T(x, t_{\text{scale}}) = \frac{l_\perp^4}{\omega_\parallel t_{\text{scale}} \Lambda_T^5} g_{5/2}(ze^{-\beta m x^2/2t_{\text{scale}}^2}). \tag{5.56}$$

Note that for interacting clouds the treatment is not so straightforward (see Sec. 5.5). Note also that for 1D clouds the semiclassical treatment of the radial momentum distribution will fail.

5.4 Quasi-condensate as nonideal atomic beam

A quasi-condensate, at a temperature below $\sqrt{\gamma}T_d$, can be described as a macroscopic wavefunction obeying the Gross-Pitaevski equation [Eq. (2.30)] with a stable Thomas-Fermi like density profile but a phase that fluctuates along the symmetry axis [77] as was discussed in Sec. 2.4.4. The macroscopic wavefunction can be written as

$$\Psi_Q(x) = \sqrt{n_l(x)} e^{i\phi(x)}, \tag{5.57}$$

where n_l is the linear atomic density obeying Eq. (2.36). This quasi-condensate wavefunction is governed by inter-atomic interactions until its release from the trap when the interaction energy vanishes almost instantaneously (see Sec. 5.5 and references there). From that time onwards the atomic wave is well described by the linear Schrödinger equation in 1D, Eq. (5.19) and we can apply the ABCD formalism for matter waves to study its behavior. Note that the normalization of Ψ_Q is such that $\int |\Psi(x)|^2 dx = N$, the total particle number.

While the density of the 1D quasi-condensate is stable, the phase can fluctuate. Low energy excitations of elementary modes in the energy range $\hbar\omega_\parallel < \varepsilon \lesssim \mu$ result in an increased axial momentum spread. The excitations, that obey the Bogoliubov-de Gennes equations, with an energy spectrum given by Eq. (2.39) have a Bose distribution [Eq. (2.11) and $\mu = 0$]. The $k = 0$ mode of this spectrum is simply the ground state that has an arbitrary constant phase. All higher modes are

orthogonal to the ground state mode and have zero spatial average. The wavevector k counts the number of nodes in the corresponding mode.

In order to find the relation between the quasi condensate temperature and its width at the time of focus we exploit the analogy between the quasi-condensate matter wave Ψ_Q and the nonideal optical beam of Sec. 5.2.2. Following Riou *et al.* [146, 148] we have given the quality factor M^2 for matter waves in Eq. (5.35). Equation (5.34) showed that M^2 is invariant under linear ABCD transformations. We extend the work by Riou here by giving a physical interpretation of the quality factor by relating M^2 to the quasi-condensate temperature. We have seen in Sec. 5.3.2 that our focusing procedure is composed of a rotation followed by a shearing deformation of the Wigner chart. Figure 5.5 shows a schematic representation of the focusing process. An initial BEC in a cigar shaped trap has a large spatial extent and a small momentum spread [Fig. 5.5(a)]. The application of a harmonic potential pulse with frequency ω and duration t_p, performs a rotation with an angle $\theta = \omega t_\mathrm{p}$ [Fig. 5.5(b)]. Free evolution, finally, performs a shearing deformation. The focus is reached when Δx reaches its minimum: $\hbar\Delta k/m\omega\sin\theta$ [Fig. 5.5(c)]. At t_in the

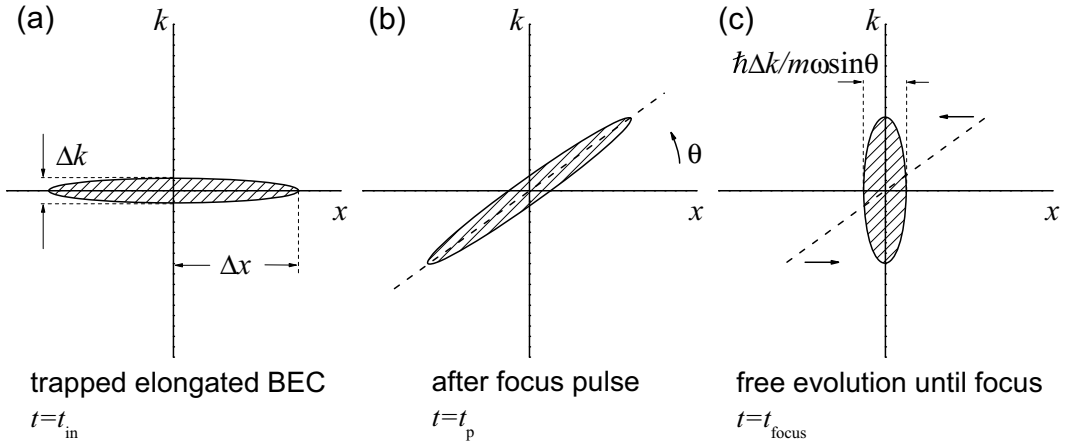

Figure 5.5: Schematic representation of the focusing process as a deformation of the WDF. (a) An initial BEC in a cigar shaped trap has a large spatial extend and a small momentum spread. (b) The application of a focussing pulse performs a rotation with an angle θ. (c) Free evolution performs a shearing deformation. The focus is reached when Δx reaches its minimum $\hbar\Delta k/m\omega\sin\theta$.

WDF of the equilibrium quasi-condensate at rest is aligned with both the position and momentum axes; i.e., there is no correlation between position and momentum, hence the mixed moment $\Delta_{xk} = 0$. Therefore, we can simplify Eq. (5.35) as

$$\frac{M^2}{2} = \Delta x(t_\mathrm{in})\Delta k(t_\mathrm{in}). \tag{5.58}$$

The axial momentum width $\Delta p(T)$, that is broadened by the thermal fluctuations of the phase, is expressed by the second-order moment of the projection of the WDF of Ψ_Q. A calculation of Δp for a harmonically trapped cloud, from the phase

fluctuation spectrum employing the local density approximation, was performed by Gerbier *et al.* [74, 169], who find the approximate relation

$$\Delta p^2(T) \approx \left(\frac{\alpha\hbar}{L}\right)^2 + \left(\frac{\beta\hbar}{l_\phi(T)}\right)^2, \tag{5.59}$$

with $\alpha = 2.0$, $\beta = 0.65$ and where the phase coherence length l_ϕ is inversely proportional to the temperature. The phase coherence length is given for the 1D homogeneous case by Eq. (2.40). For a harmonically trapped condensate in the 3D to 1D cross-over l_ϕ can be conveniently expressed as a function of the peak linear density $n_l(0)$ [74] if the local density approximation is employed

$$l_\phi = \frac{\hbar^2 n_l(0)}{m k_B T}. \tag{5.60}$$

The quasi-condensates in the experiments discussed in this chapter have $T \approx 10^2$ nK and $n_l(0) \approx 10^2\ \mu\text{m}^{-1}$. For these numbers Eq. (2.40) yields $l_\phi \approx 6\ \mu$m; much smaller than the cloud length $L \approx 10^2\ \mu$m. Equation (5.59) then simplifies to

$$\Delta p = \hbar\Delta k = \frac{\beta\hbar}{l_\phi}. \tag{5.61}$$

Equation (5.58) relates the momentum width, Eq. (5.61), to the M^2 factor. We write $\Delta x(t_{\text{in}}) = \kappa L$ and arrive at

$$M^2 = 2\beta\kappa\frac{L}{l_\phi}, \tag{5.62}$$

where $\kappa \approx 1/\sqrt{5}$ for our typical parabola-like clouds.

Equation (5.62) allows us to express relation (5.48) explicitly as a function of the phase coherence length. We arrive at the expression for the free-space propagation of a phase-fluctuating quasi-condensate

$$\Delta x^2(t) \;=\; \Delta x_0^2\left[1 + \left(2\beta\kappa\frac{L}{l_\phi}\right)^2\left(\frac{\hbar}{2m\Delta x_0^2}\right)^2 (t - t_{\text{focus}})^2\right]. \tag{5.63}$$

In Sec. 5.6 we use Eq. (5.63) in a model to fit our experimental results. This will allow us to determine l_ϕ, and subsequently to extract the temperature of the quasi-condensate from Eq. (5.60).

5.5 Weakly interacting condensate in a time dependent trap

The treatment of quasi-condensate propagation that was given in the previous section holds in the limit of vanishing interatomic interactions. In this section we treat the first part of the focusing process including interactions. We study the

time evolution of a trapped (quasi-)condensate in a changing harmonic potential. Three-dimensional trapped condensates respond differently to a change in potential as compared to the 1D trapped case. Our condensates are in the cross-over from 3D to 1D. It will be shown however that for small evolution times (our condensate is released shortly after the change in harmonic potential) the 3D and 1D solutions give quantitatively very similar results.

The trapped three-dimensional condensate has a parabolic shape in all spatial dimensions, see Sec. 2.4.1. The evolution of the cloud size can be described with scaling solutions [156–158]. We follow the notation of Castin and Dum [156]. The key point of this approach is that a parabolic cloud shape is maintained if the strength of the harmonic potential is changed in time. In particular, if the cloud is suddenly released from the trap it will expand maintaining its parabolic shape. The scaled cloud size b_i in direction $i = x, y, z$ evolves like

$$\ddot{b}_i = \frac{\omega_i^2(0)}{b_i(t)b_x(t)b_y(t)b_z(t)} - \omega_i^2(t)b_i(t). \tag{5.64}$$

In Sec. 5.6 we will show a numerical solution of (5.64) for our experimental focus pulse $\omega_\parallel(t)$, for the case of the 3D cigar with $\omega_\parallel \equiv \omega_x >> \omega_y = \omega_z \equiv \omega_\perp$. Here we consider a sudden opening of a cylindrically symmetric trap at $t = 0$, Eq. (5.64) then simplifies to

$$\begin{aligned} \frac{d^2}{d\tau^2}b_\perp &= \frac{1}{b_\perp^3(t)b_\parallel(t)}, \\ \frac{d^2}{d\tau^2}b_\parallel &= \frac{\epsilon^2}{b_\perp^2(t)b_\parallel^2(t)}, \end{aligned} \tag{5.65}$$

where we have introduced the dimensionless time parameter $\tau = \omega_\perp(0)t$ and the small inverse aspect ratio $\epsilon = \omega_\parallel(0)/\omega_\perp(0) \ll 1$. To zeroth order in ϵ, sufficient for our experiments with $\epsilon \approx 1/400$, we find the solution for Eq. (5.65): $b_\parallel = 1$, i.e. the axial expansion of the cloud is negligible. The radial expansion scales as

$$b_\perp(\tau) = \sqrt{1 + \tau^2}, \tag{5.66}$$

and grows linearly for $t \gg \omega_\perp^{-1}$, i.e. shortly after release. We solve Eq. (5.64) numerically for more complicated, realistic temporal potential changes. An example is given in Fig. 5.6 where the red curves correspond to the shape oscillation in a 3D cloud that would appear if the focus pulse (an increase of the axial trapping frequency by a factor of three at $t = 0$) would be left on indefinitely. This results in large anharmonic amplitude oscillations showing the nonlinear character of the system. There is a visible difference between the periods of these large oscillations and that of small harmonic amplitude oscillations that have a quadrupole frequency $\omega_Q = \sqrt{5/2}\omega_\parallel$ (dashed red lines in Fig. 5.6) [170]. The condensates in our experiments are in the cross-over from the 3D to the 1D regime. This alters the scaling equation. In the 1D limit the axially compressed condensate will remain in the radial ground state as long as the axial dynamics is slow compared to the radial trap

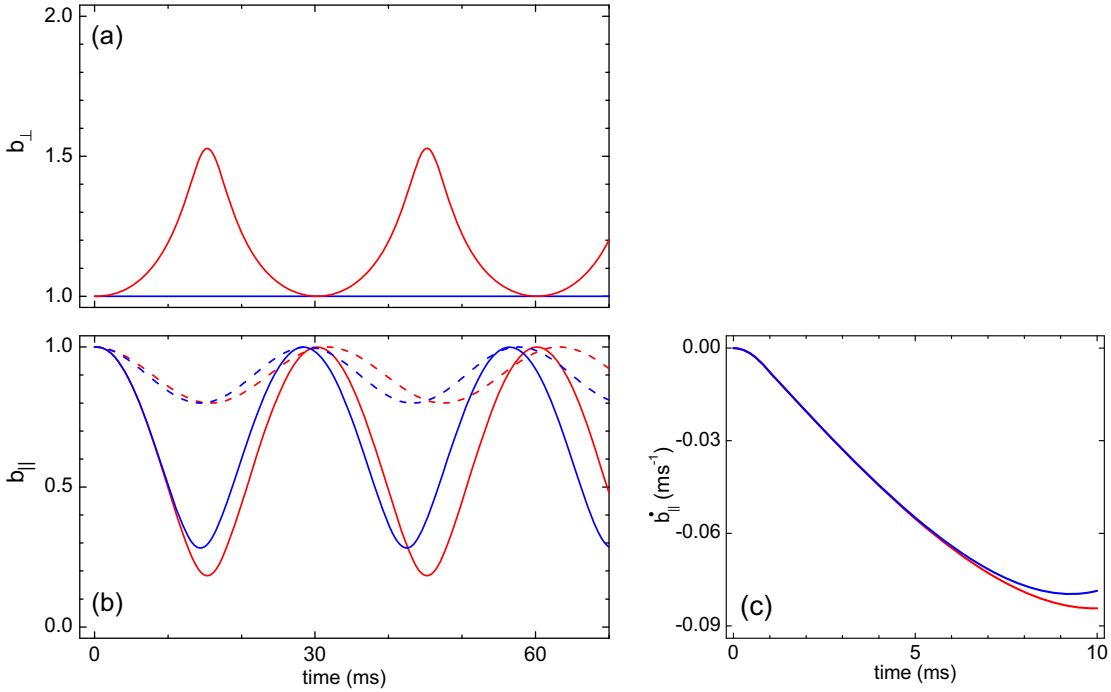

Figure 5.6: Large amplitude oscillations of an elongated BEC in a harmonic trap shows nonlinear behavior; red lines are solutions for the 3D case, the 1D solutions are drawn in blue. (a) Scaled radial size. (b) Scaled axial sizes dotted lines indicate the solutions in the limit of small oscillation amplitudes yielding $\omega_Q = \sqrt{5/2}\omega_\parallel$ in 3D and $\omega_Q = \sqrt{3}\omega_\parallel$ in 1D. (c) A comparison of the axial inward velocity for 3D and 1D directly after the start of an oscillation shows that the difference is negligible in the first 5 ms.

frequency and the interaction energy is negligible compared to the radial vibration energy $\mu \ll \hbar\omega_\perp$. In that limit the scaling equation reads

$$\ddot{b}_\parallel = \frac{\omega_\parallel^2(0)}{b_\parallel^2(t)} \left(\frac{\omega_\perp(t)}{\omega_\perp(0)} \right)^4 - \omega_\parallel^2(t) b_\parallel(t). \tag{5.67}$$

Figure 5.6 shows a comparison of the 1D and 3D results. The blue dashed line indicates the quadrupole frequency $\omega_Q = \sqrt{3}\omega_\parallel$ expected for small-amplitude oscillations. In Fig. 5.6(c) we plot $\dot{b}_\parallel$ for the 1D and 3D case. For our focusing pulse of 5.4 ms (see Sec. 5.6), that is much shorter than the axial harmonic oscillator time, the difference between the inward velocity for the 1D and the 3D solution is negligible. We calculate a focus time for the 1D case that is only 0.3% longer than that for the 3D case. We model a sudden release from the trap by $\omega_\perp \to 0$ at the time of release thus cancelling the first term on the right hand side of Eq. (5.67) from the time of release onwards.

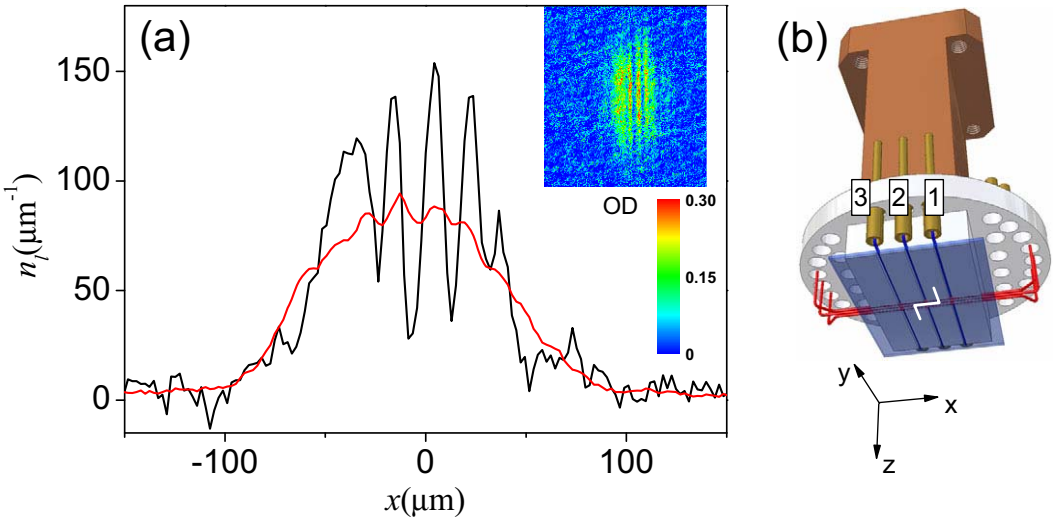

Figure 5.7: (a) Linear density of an elongated Bose gas after 20.5 ms of free expansion. Each single realization shows strong random density modulations, while the average density distribution is smooth and reproducible. An example single realization is shown in black, and the inset shows the corresponding optical density image before integration along z. The density distribution found after averaging 50 images is shown in red. The final frequency of the evaporation RF is 1.53 MHz for these images. (b) Our magnetic microtrap configuration, indicating the Z-wire on the atom chip, the two orthogonal sets of three miniwires, and the orientation of the frame of reference.

5.6 Experiments

The experimental procedure for the quasi-condensate focusing experiments starts with the generation of an elongated degenerate cloud as described in Sec. 4.2.7. For a final RF frequency of 1.53 MHz we have an almost pure quasi-condensate with an atom number of $8 \cdot 10^3$ and a linear density in the trap center of 80 μm^{-1}, corresponding to $\mu \approx 0.6\hbar\omega_\perp$, i.e. on the 1D side of the dimensional cross-over ($\omega_\perp/2\pi = 3.28$ kHz, $\hbar\omega_\perp/k_B = 158$ nK, as stated in Sec. 4.2.7). We perform three types of measurements on the gas using absorption imaging in *time-of-flight* (after free fall from the trap), *in situ* (in the trap), and *focus* (after the application of a focusing pulse). We vary atom number and temperature of the gas by changing the final RF frequency. The gas is probed using absorption imaging with circularly polarized light resonant with the $|F = 2\rangle \rightarrow |F' = 3\rangle$ transition of the ^{87}Rb D2 line at one third of the saturation intensity. For the time-of-flight and *in focus* data described below, the quantization axis is defined by a small magnetic field of $B_y = 2$ G along the imaging axis, and the illumination time is 80 μs. For the *in situ* measurements a shorter pulse of 20 μs is used to reduce blur due to heating of the atoms from photon recoil.

We start the description of our results with the time-of-flight data. A typical absorption image, and the resulting linear density along the axis is shown in Fig. 5.7(a). Each individual realization shows strong density fluctuations (black line), while averaging over 50 images result in a smooth distribution (red line). These fluctuations

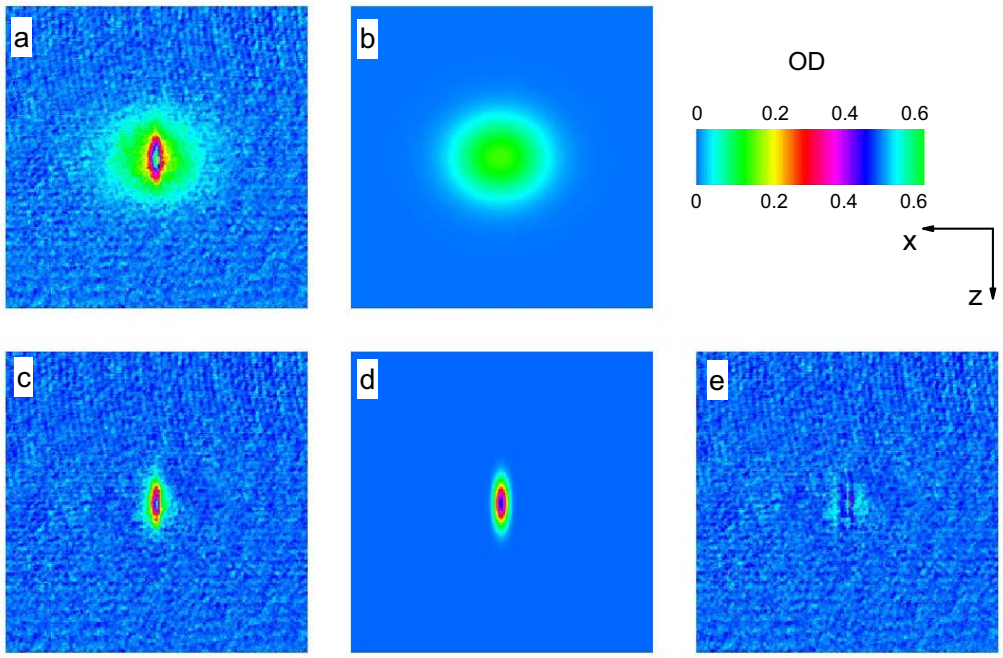

Figure 5.8: Fits to an average over 8 absorption images of a bimodal cloud during focusing. (a) Absorption image corresponds to final RF frequency of 1.57 MHz and a time of 17.3 ms after the start of the focus pulse. (b) Gaussian fit to thermal part, central area is excluded from the fit. (c) Data with fitted pedestal subtracted. (d) Gaussian fit to the central peak after subtraction of the pedestal. (e) Residue of the fit. The color coding of the optical density is indicated with a scale bar, each image size is 430×430 μm^2.

develop from the initial phase fluctuations of the degenerate gas and have been studied in detail for elongated 3D condensates with $\mu > \hbar\omega_\perp$ [171–173]. Images like these clearly establish the phase-fluctuating character of our one-dimensional atom clouds corresponding to $M^2 \gg 1$. A quantitative analysis of the axial density fluctuations is cumbersome, a point we will come back to in Sec. 5.8. Furthermore, the radial expansion, visible in the z direction, is also of limited use for characterizing temperature and chemical potential in our regime of $\mu < k_B T$ and $k_B T \approx \hbar\omega_\perp$, because the radial expansion is then dominated by the radial ground-state energy [39]. As we will now discuss, much more information can be readily obtained from the *focus* data.

The magnetic focusing pulse is created by ramping up the axial trapping frequency from 8.5 Hz to 20 Hz in 0.8 ms, maintaining this for 3.8 ms, and ramping back down to 8.5 Hz in 0.8 ms, as is illustrated in Fig. 5.9. The axial trapping potential is changed by sending a current of (5, -0.23, 5)A through miniwires 1, 2 and 3 respectively [see Fig. 5.7(b)]. This is followed by a sudden switch-off of the magnetic trap. During the focusing pulse the cloud length reduces by only 15%, see Fig. 5.6. After switching off the magnetic trap, the cloud expands in the radial direction on a timescale of $1/\omega_\perp$ (cf. Sec. 5.5), so that the interactions vanish rapidly

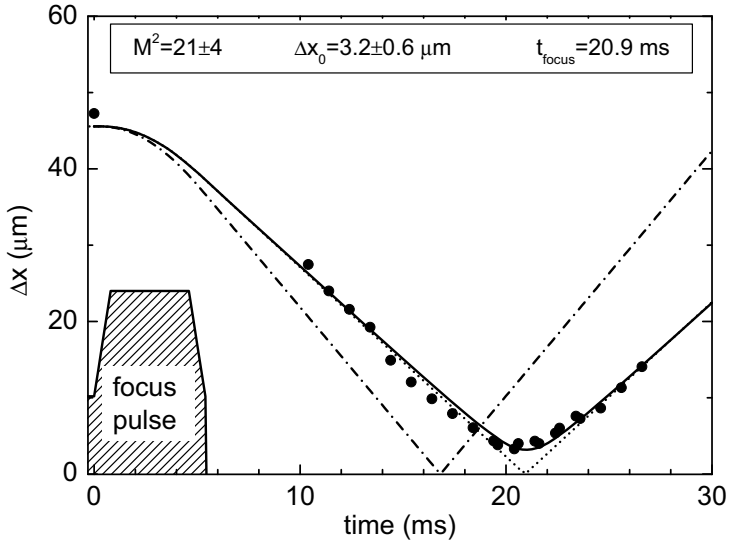

Figure 5.9: Experimental focus data (•) and calculated axial cloud size for a BEC using the scaling solution (dotted line). A more realistic model based on the scaling solution during the focus pulse and the nonideal gaussian matter wave during free flight was fitted to the experimental data (straight line). For comparison we show the the classical trajectory of a point particle starting at rest calculated with the ABCD formalism (dash-dotted line). The timing of the axial potential pulse is indicated as the shaded area.

compared to the relevant axial timescale and the subsequent axial contraction can be treated as free propagation. After a free propagation time of ≈ 15 ms the cloud comes to an axial focus.

As an example, Fig. 5.8 shows an absorption image of a partly condensed cloud taken 17.3 ms after the start of the focus pulse corresponding to a final RF frequency of 1.57 MHz; we have averaged over 8 images. We perform a bimodal gaussian fit to the 2D atomic density distribution and extract atom number and axial and radial dimensions of the thermal and condensed parts of the bimodal cloud. The axial shape of the quasi-condensate upon focusing changes from approximately parabolic in the trap (see Sec. 2.4.3) to an approximately Lorentzian shape in the focus as was shown in Ref. [169]. In addition to that, the focal shape is blurred by the finite resolution limit of our detection optics. To treat density distributions with arbitrary shapes we measure the second-order moment [Eq. (5.30)] of the axial density. In practice, we do this by fitting the axial density distribution with the gaussian function $a\exp[-x^2/2\Delta x^2]$, where Δx is the second-order moment of the fitted Gaussian distribution. This procedure is expected to give good estimates for the position spread in the focal region where the atomic density distribution is well approximated by a gaussian, while it would overestimate the second-order moment for a trapped pure quasi-condensate profile [Eq. (2.36)].

We use the following hybrid model to describe the complete time evolution of a quasi-condensate during the focusing process. For the first part, the quasi-

condensate in the trap during a focusing pulse, we use the scaling equations (Sec. 5.5). We numerically integrate the scaling equations for our exact values of $\omega(t)$. Subsequently, to model the free evolution after release from the trap, we use the nonideal atomic beam description [Eq. (5.63)]. We match the two parts by calculating the cloud size $\Delta x(t_\mathrm{p})$ and inward velocity $\Delta\dot{x}(t_\mathrm{p})$ at the end of the focus pulse ($t = t_\mathrm{p}$) from the scaling equations and impose these as boundary conditions for Eq. (5.63). These boundary conditions fix the "far-field divergence" of the matter wave and thereby the relation between M^2 and Δx_0, leaving only a single free fitting parameter.

In Fig. 5.9 we show experimental focus data for an almost pure quasi-condensate of $8 \cdot 10^3$ atoms, corresponding to a final RF frequency of 1.53 MHz; each data point is obtained from a gaussian fit to an average over three absorption images. We fit the experimental data with the hybrid model (straight line) based on the scaling solution during the focus pulse and the nonideal matter wave, after that [Eq. (5.63)]. Indicated with the dotted line is the result of the scaling equation alone for a quasi-condensate. For comparison we show the classical trajectory of a point particle starting at rest calculated with the ABCD formalism (dash-dotted line). The timing of the axial potential pulse is indicated as the shaded area. The focus time resulting from the scaling equations is $t_\mathrm{focus} = 20.9$ ms. The fit results in $\Delta x_0 = 3.2 \pm 0.6$ μm and $M^2 = 21 \pm 4$. Assuming that M^2 is constant during the focus pulse, and with the peak linear density obtained from the *in situ* data, $n_l(0) = 80$ $\mu\mathrm{m}^{-1}$, we find from Eq. (5.62) and Eq. (5.60) $T = 0.16 \pm 0.04$ μK.

In Fig. 5.10 we show the fit results for the partly condensed cloud, for a final RF frequency of 1.57 MHz (as in Fig. 5.8) corresponding to a thermal cloud containing $N_\mathrm{ex} = 5.5 \pm 0.3 \cdot 10^3$ and a condensed part of $N_0 = 1.3 \pm 0.1 \cdot 10^3$. The thermal cloud radial expansion ($\diamond$) is approximately linear for $t \gg \omega_\perp^{-1}$ [Eq. (5.66)], while the axial size shows the effect of focusing ($\bullet$). The much smaller axial size of the condensed part is indicated with ($\triangle$). From a fit to the radial expansion of the thermal part we extract $T = 0.46 \pm 0.01$ μK. We calculate the axial size for this temperature with Eq. (5.53) and find the drawn black curve. The measured axial size at $t = 0$ clearly exceeds Δx_T [Eq. (5.36)] of an ideal Boltzmann gas. We attribute the broadening to the repulsive force of the non-negligible atomic interactions in the trap. We have modelled the effect of interactions using a reduced effective initial potential $V_\mathrm{eff} = m\omega_\mathrm{eff}^2 x^2/2$ with $\omega_\mathrm{eff} = 6.7\ \mathrm{s}^{-1} < \omega_x$ to match the calculated and measured initial sizes. If we calculate the propagation of the cloud width upon applying the same focus potential as before we obtain the dashed line in Fig. 5.10. The dash-dotted line indicates a fit to the central peak using the hybrid model where we have not only used Δx_0 as fitting parameter but have additionally let t_focus free in the fitting process. The resulting focus time is 18.1 ms, shorter than the 20.9 ms that we find for condensates of $8 \cdot 10^3$ atoms. We discuss this effect of a reduced focus time in Sec. 5.7.

In practice we have measured the *in focus* distribution at a fixed time $t = 20.9$ ms. Figure 5.11 shows results of *in focus* measurements when we lower the final RF frequency. In Fig. 5.11(a) we show the cloud temperatures determined from the quasi-condensate focal width ($\triangle$). The error bars are estimated based on the finite

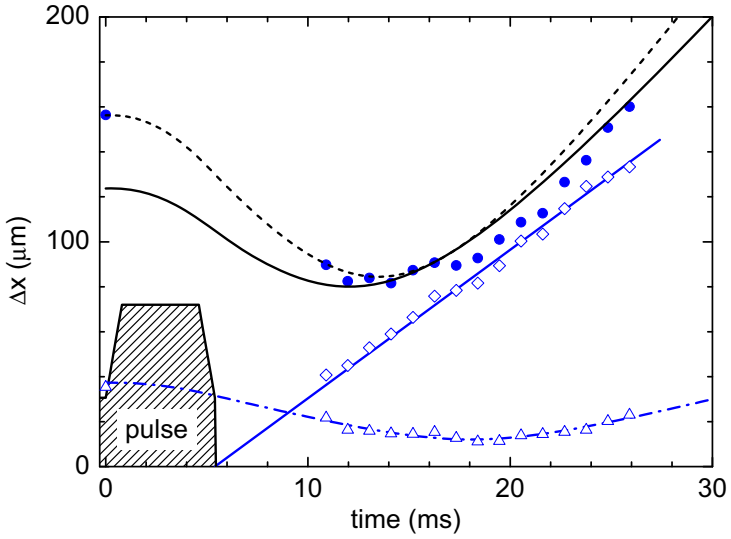

Figure 5.10: Experimental focus data for the thermal and condensed parts of a partially condensed cloud. The thermal cloud radial expansion (◇) is approximately linear for $t \gg \omega_\perp^{-1}$, while the axial size is clearly focussed (●). The much smaller axial size of the condensed part is indicated with (△), the dash-dotted line is the result of a fit using a hybrid model (see text). From a fit to the radial expansion of the thermal part we extract $T = 0.46 \pm 0.01$ μK. We calculate the axial size for this temperature and find the drawn (dotted) curves when we neglect (include) the repulsion of the thermal atoms by the condensate in the trap.

optical resolution of $\Delta x = 2.8 \pm 0.6$ μm and on a 20% error in Δx_0 as found in the fit of Fig. 5.9. We compare the results with a temperature determined from the radial expansion energy of the thermal pedestal of the bimodal clouds (◇). In the latter temperature determination, the contribution to the expansion energy from the ground state has been neglected. The dash-dotted line is to guide the eye and indicates a ratio of 11 of the trap depth (set by $\omega_{\rm RF}$) and the cloud temperature. The dashed line corresponds to $\hbar\omega_\perp/k_B$. In Fig. 5.11(b) we show the atom number in the condensate (△) and in the thermal component (●). We discuss here the discrepancies between the two presented temperature measurements. We expect that the radial expansion data overestimate the temperature for $T \lesssim \hbar\omega_\perp$ where the radial size is dominated by the size of the harmonic oscillator ground state. On the other hand, for the central peak width, we have seen in Fig. 5.10 that the focus time shifts towards lower values for degenerate clouds at higher temperatures and lower linear densities indicating deviations from the quasi-condensate model that can be the reason for the deviating results for $\omega_{\rm RF} \gtrsim 1.55$ MHz. The presence of density fluctuations can explain the effect of a shift of the focus towards earlier times for higher final RF values as will be discussed below (see also Ch. 6).

It was shown in Fig. 5.9 that the quasi-condensate focusing description works fine for condensates with atom numbers $\sim 8 \cdot 10^3$. For lower atom numbers, however, we see deviations as is illustrated by the observed reduced focus time for condensates

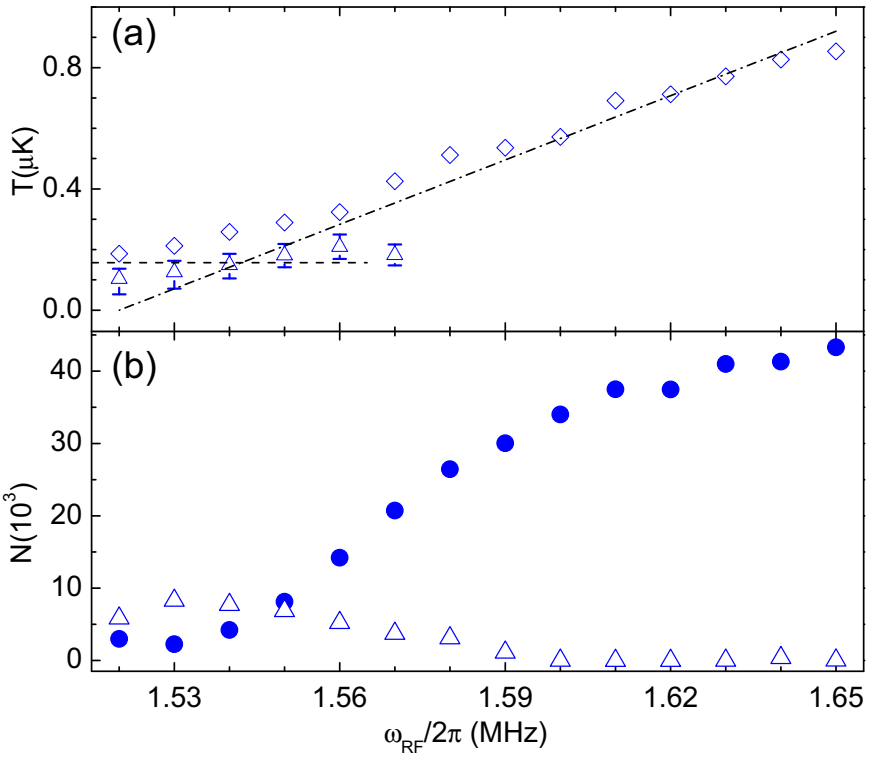

Figure 5.11: Characterization of the measured atomic clouds as a function of the final RF frequency ω_{RF}, as determined from Gaussian fits to the *in focus* data. (a) Temperature from the radial (◇) size of the broad Gaussian fit to the *in focus* data. The dash-dotted line is to guide the eye and indicates a ratio of 11 of the trap depth (set by ω_{RF}) and the cloud temperature. The dashed line corresponds to $\hbar\omega_{\perp}/k_B$. (b) Atom number from the *in focus* data: wide distribution (●) and central peak (△).

with lower atom number (triangles in Fig. 5.10). Figure 5.12 shows focus traces for varying atom number for the same final $\omega_{\mathrm{RF}} = 1.52$ MHz of the evaporation trajectory, each datapoint comes from a gaussian fit to an absorption image averaged over typically 4 images. For comparison the focus data for $N = 8 \cdot 10^3$ presented in Fig. 5.9 are also plotted (black). We reduce the atom number by reducing the duration of the first part of the RF evaporative cooling ramp, while leaving the last part of the ramp unchanged. When the atom number is lowered we observe that the time of narrowest waist comes earlier. Additionally the waist size increases with decreasing atom number.

5.7 Discussion

The observed reduced focus time and increased focal width when the atom number is lowered, as presented in Fig. 5.12, likely stem from deviations in the degenerate cloud during the focus pulse from the mean-field description. This can be qualitatively understood in the following way: Although our experimentally observed clouds are

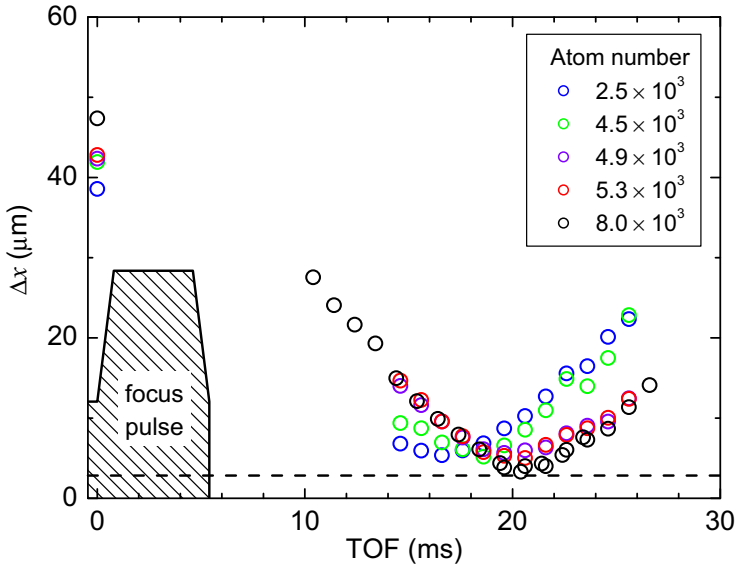

Figure 5.12: Experimental focus data for varying atom number. When the atom number is intentionally decreased we observe that the time of narrowest waist comes earlier. Atom numbers are indicated in the legend. The dashed line indicates the resolution limit.

in the cross-over from 3D to 1D we can best understand the effects of reduced coherence by considering the pure 1D case, corrections for the cross-over case do not qualitatively change the argument. When the atom number is lowered, even at constant temperature, the chemical potential decreases, cf. Fig. 2.2. As a result, the relative importance of the density fluctuations increases as is also visible in Fig. 2.2: Decreasing μ for constant finite temperature leads to an increasing two-particle local correlation $g^{(2)}$. We conclude that, by reducing the atom number at constant temperature, we enter the regime where $T \gtrsim \sqrt{\gamma} T_d$ (see Sec. 2.6.2) and the local value of $g^{(2)}$ becomes larger than 1. This means that the atomic density fluctuates and that the quasi-condensate starts to behave more and more like a decoherent thermal cloud. This results in a broadened focus that moves to earlier focus times as the coherence is reduced. The reduced focus time for decoherent clouds can also be seen in Fig. 5.9 by comparing the dotted line for a quasi-condensate with the dash-dotted line for non-interacting particles. In Ch. 6 we present a more detailed quantitative description of this reduced coherence based on the Yang-Yang thermodynamics.

We observe very narrow density distributions with Δx waists down to 3 μm. These small features are close to the resolution limit of our optical system, see Sec. 3.9. The optical resolution could be improved, for example, by placing an objective lens *in vacuo* or outside a new and smaller vacuum system.

5.8 Conclusion and outlook

We have presented a model that describes the propagation of a quasi-condensate when it is focused in free flight. This model enables us to quantitatively extract the temperature of a phase-fluctuating quasi-condensate from the atom-beam quality factor M^2. We have thus implemented a quasi-condensate thermometer. The temperature of the quasi-condensate is a direct measure of the phase coherence. By measuring the momentum spread of a focused quasi-condensate we probe the first-order correlation function. These correlations are the fundamental ingredient for the collective behavior of degenerate gases and of importance in possible applications of coherent matter waves like the guided-wave atom-interferometer [96].

We have also seen deviations from the quasi-condensate description in the regime where the mean-field approach is not valid, i.e. for low linear atomic density and relatively high temperature so that $T \gtrsim \sqrt{\gamma} T_d$. We will show in Ch. 6 that especially in this regime of reduced coherence the focus method is very useful to provide information on the correlations in the gas.

As was mentioned in Sec. 5.6 the analysis of the phase fluctuations after time-of-flight is cumbersome. The difficulties stem from the large modulation depth of the density fluctuations as shown in Fig. 5.7(a). We therefore can not use the analysis method developed by Petrov *et al.* [77, 171]. As an outlook we suggest a possible alternative approach, that we have tested preliminarily: A phase reconstruction method. This method is based on the description of the quasi-condensate as a matter wave, like light in the paraxial approximation. Employing the continuity equation it is possible to reconstruct the phase of a general wave in 1D from two measurements of the density distribution of this wave taken shortly after one another [174,175]. In practice, we can not take two subsequent images of the same cloud because of the destructive absorption imaging method. However we know from theory and repeated measurements that the *in situ* density distribution is smooth and reproducible from shot to shot. The constant *in situ* density distribution can therefore serve as the first density measurement. Single *time-of-flight* density measurements could then be sufficient to reconstruct the phase of the matter wave. The implementation of this method and the analysis of its range of validity are beyond the scope of this thesis but form a nice outlook for further study.

Another topic for further study could be to use extensions of the ABCD formalism to describe a (trapped) weakly interacting gas. One could make use of an extended ABCD formalism that was given by Paré and Bélanger [176] to model light propagation in non-linear (Kerr) media. Additionally, a recent preprint by Impens and Bordé attacks the same problem [177].